# Microstructure dependence of performance degradation for intermediate temperature solid oxide fuel cells based on metallic catalyst infiltrated La- and Ca-doped $SrTiO_3$ anode support

C. S. Ni†, L. Y. Lu†, D. Miller, M. Cassidy and J. T. S. Irvine*
School of Chemistry, University of St Andrews
KY16 9ST, St Andrews, United Kingdom
*jtsi@st-andrews.ac.uk

†Ni and Lu are equal contributors to this work.

## Abstract

Anode-supported solid oxide fuel cells with the configuration of $La_{0.2}Sr_{0.25}Ca_{0.45}TiO_3$ ($LSCT_{A-}$) anode, YSZ electrolyte and $La_{0.8}Sr_{0.2}Co_{0.2}Fe_{0.8}O_3$ (LSCF)-YSZ cathode were fabricated using tape casting and co-sintering techniques followed by pre-reduction and impregnation. In order to improve the performance, the active anodes were prepared via the wet impregnation of metallic catalysts (Ni or Ni-Fe solution). The impregnation of 3 wt.% nickel significantly improved the fuel cell performance from 43 $mW/cm^2$ for the bare $LSCT_{A-}$ anode to 112 $mW/cm^2$ for the Ni-$LSCT_{A-}$ anode at 700 $^oC$ in humidified hydrogen containing 3 vol.% $H_2O$. More interestingly, the substitution of 25 wt.% Fe to Ni further enhances the power density by a factor of 2.5, compared to the Ni-impregnated cell. The cell infiltrated with Ni-Fe solid solution shows a slower degradation than the other two cells after the first 20-h period. High-resolution back-scattered electron (BSE) and transmission electron microscopy (TEM) images performed on the cross section of the impregnated anodes with time after ion beam preparation show that the sintering of the catalyst particles on the scaffold surface and the interaction between backbone and catalyst are the predominant contributions for the degradation of cell performance.

## Introduction

Solid oxide fuel cells are electrical generation devices that convert the chemical energy directly into electricity through the electrochemical reaction between a fuel and an oxidant. They have been considered as the most efficient, cleanest power-generation systems[1,2], offering the great prospects for the direct utilization of a wide variety of hydrocarbon fuels[3~5]. The most commonly used anode material in SOFC is the porous Ni-YSZ cermet, usually used in conjunction with an yttria-stabilised zirconia (YSZ) electrolyte. The nickel provides both the electronic conducting pathways and the electrocatalytic activity for fuel oxidation, the YSZ acts as the oxygen ionic conductor and provides a measure of structural stability[6,7]. However, Ni-YSZ anodes were found to show serious degradation when using hydrocarbon as fuel due to carbon deposition[8] and sulphur poisoning[9]. The degradation of Ni-YSZ anode is also aggravated by the agglomeration and sintering of nickel particles under the operation condition[10], which is the critical issue limiting the development of Ni-YSZ cermet anode.

To overcome the problems related to the Ni-YSZ anode, A-site doped strontium titanate based perovskites have been developed owing to their high electronic conductivity and good volumetric stability in reducing atmospheres[11~13]. In the earlier work, La-substituted $SrTiO_3$ (LST) exhibited a high electrical conductivity over 100 S/cm in reducing atmosphere[14] after a pre-reduction at elevated temperatures. However, LST was known to exhibit a limited ionic conductivity and a poor catalytic activity for fuel oxidation[15]. These weaknesses could be compensated by infiltration of metal catalyst as well as an ionic conductor, such as GDC, into the perovskite scaffold. Remarkable performance has been reported using A-site deficient titanate-based anode infiltrated with nickel, copper or ruthenium with additional ceria phase[16~19]; for example with Ni and $CeO_2$-impregnated pre-reduced $La_{0.2}Sr_{0.25}Ca_{0.45}TiO_3$ ($LSCT_{A-}$) anode composite, a power density of 960 $mWcm^{-2}$ was achieved at 800 $^oC$ for the cells when humidified hydrogen was used as fuel[19].
For an SOFC working continuously for forty-thousand hours, a high durability is critically important, especially for electrodes with nano-particles via infiltration method[20]. The reason for the degradation of an electrode prepared by infiltration has been so far ascribed to the morphology variation of the impregnated coatings on the scaffold surface that leads to the decrease of effective reaction sites, as seen extensively during stability testing of cathode materials[21~23]. Similarly, for the titanate perovskite anode, a strong degradation was also observed and has been mainly attributed to the increase of polarization resistance[24,25]. For example, a short-stack electrolyte-supported based on $LSCT_{A-}$ anode of 100 $cm^2$ has been tested at 800 $^oC$ and 900 $^oC$ and severe degradation of cells has been observed though an initial power output of 3.3 kW has been obtained[26]. However, the interaction between the titanate scaffold and the impregnates has never been studied. It has been known that YSZ scaffold structure could be modified by treatment in hydrofluoric acid[27], therefore titanate might topographically react with the nitrate solution during impregnation and the subsequent firing process. This in turn may affect the subsequent interaction between titanate and catalytic metal during the operation of anode and provide an alternative mechanism for the degradation. Therefore, an in-depth survey on the infiltrated anode is required, allowing an improved understanding of the microstructure-performance relationship not only on the catalyst morphology but also on the scaffold-catalyst interfacial reaction. We utilised a focussed ion beam (FIB) sectioning and polishing technique for cross-section preparation to reveal the interface between the catalyst and titanate. As it is very difficult to reveal the interaction between impregnates and scaffolds on the surface morphology the ion preparation techniques have the advantage of minimising surface damage associated with mechanical techniques and offer the possibility of revealing the sub-micron scale detail that occurs underneath the surface of this interface.[28] For the first time we found that the interior morphology near the surface after the annealing process would be playing an important role in the degrading mechanism. In this paper, we present some stability studies on $LSCT_{A-}$ anode-supported fuel cells with Ni or Ni-Fe infiltrated into the anode, and try to understand the mechanism for the degradation via the high-resolution

back-scattered electron (BSE) and transmission electron microscopy (TEM) on the cross-section of the the ion beam etched samples.

## Experimental

$La_{0.2}Sr_{0.25}Ca_{0.45}TiO_3$ ($LSCT_{A-}$) powder was supplied by Topsoe Fuel Cells as part of the EU FCH-JU project SCOTAS and was calcined at either 1100 or 1250 $^oC$ for 5 h to tailor the powder properties to obtain the compatible shrinkage process with dense YSZ, described elsewhere[19]. Button fuel cells were fabricated by an organic based tape casting technique with co-sintering of dense YSZ electrolytes bonded with porous anode and cathode skeletal structures ($LSCT_{A-}$ and YSZ respectively). To optimise the interface of the sintered $LSCT_{A-}$ anode and YSZ electrolyte, co-casting of the $LSCT_{A-}$ and YSZ green tapes was employed, where the $LSCT_{A-}$ wet tape slip was cast on the top of the thin dried YSZ green tape. After drying, the green tapes were cut into an appropriate size and laminated to form the complete cell skeletal structure, followed by co-sintering at 1350 $^oC$ in air. This process is described in greater detail elsewhere [19].The sintered samples of 2 cm in diameter were subjected to a reduction process at 900 $^oC$ for 12 h in a 5 % $H_2$-Ar atmosphere. Upon reduction, the colour of $LSCT_{A-}$ changes from light yellow to black.

The cathode side of pre-reduced samples were impregnated with precursor solutions containing $La_{0.8}Sr_{0.2}Co_{0.2}Fe_{0.8}O_3$ (LSCF) and fired at 450 $^oC$ in air to decompose the nitrate but avoiding the re-oxidation of $LSCT_{A-}$. The loadings of impregnates in the YSZ cathode were 20-25 wt.% LSCF. Anode catalyst materials including Ni and $Ni_{0.75}Fe_{0.25}$ were impregnated into the porous $LSCT_{A-}$ scaffold using solutions of $Ni(NO_3)_2.6H_2O$ (Newburyport, MA USA) for the former and with additional $Fe(NO_3)_3.9H_2O$ (Sigma-Aldrich, USA) mixed at a 3:1 mole ratio of Ni:Fe for the latter. A small addition of triton surfactant was added to aid impregnation. Multiple cycles of impregnation and calcination at 450 $^oC$ were used until the desired loading of impregnates of oxides was reached.

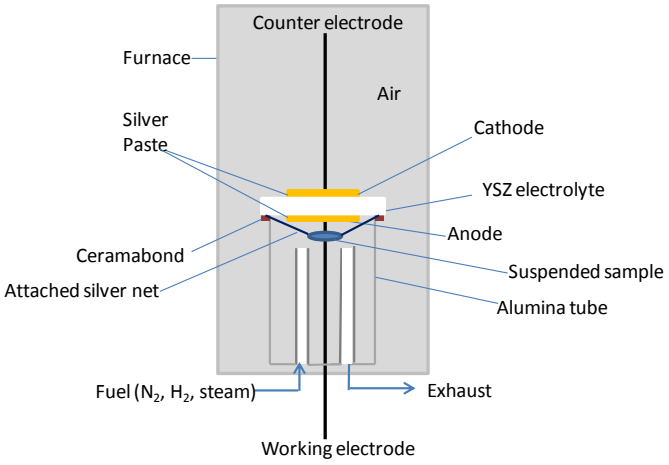


Figure 1 Schematic of simulated fuel cell operation atmosphere for reduction of metallic catalysts

In order to identify the phases obtained from the impregnated materials at different atmospheres, $Ni(NO_3)_2.6H_2O$ and $Fe(NO_3)_3.9H_2O$ were dissolved into deionised water to prepare nickel nitrate and nickel-iron nitrate solutions at a molar ratio of 3: 1 with addition of citric acid. These solutions were subsequently agitated and heated to 150 $^oC$ for combustion, followed by calcinations in air at 450 $^oC$ for 30 min, in exactly the same manner as the heat treatment of the impregnated catalysts in the porous anode scaffold. A fraction of this calcined powder was reduced at 900 $^oC$ for 12 h in a 5 % $H_2$-Ar atmosphere. The powders calcined at 450 $^oC$ in air and reduced at the atmosphere with oxygen partial pressure around $10^{-13}$ pa and 5 % $H_2$-Ar at 700 $^oC$ were characterized by XRD.

Another fraction of this calcined powder was pressed into a pellet and suspended into an alumina tube, which was sealed by a thick YSZ pellet with two silver wires attached onto two electrodes on either side. The atmosphere in the tube can be controlled by adjusting the flow rates of steam, hydrogen and nitrogen on the sealed side and the partial pressure of oxygen monitored by the OCV measured on the silver electrodes across the YSZ pellet, as shown in Figure 1. By adjusting the flow rates of the gases ($H_2$, $N_2$ and steam), an OCV value between 0.55-0.6 V versus the ambient air at the cathode side ($P(O)_2$ =0.21 atm) at 700 $^oC$ was obtained. This corresponds to an oxygen partial pressure of ~$10^{-13}$ Pa to which the calcined powder was exposed to for 12 hours.

With respect to the button cells, after the electrodes being impregnated with the precursor solutions and attached with silver wires on the electrodes, the fuel cells were directly mounted and sealed onto an alumina tube. A gas flow of Ar containing 5 % $H_2$ was passed over to the anode in order to avoid the re-oxidation of the anode upon heating to test temperature of 700 $^oC$, before switching to humidified hydrogen (3 % $H_2O$). Electrochemical tests were carried out using both DC and AC impedance techniques, the latter over the frequencies between 100 kHz and 0.04 Hz using a combination of Solartron 1255 Frequency Response Analyser and Solartron 1287 Electtrochemical Interface. To reveal the morphology samples were cut by Leica EM TIC 3X Triple Ion Beam Cutter System and were analysed by JEOL 6700 scanning electron microscopy (SEM) with energy dispersive X-ray analysis (EDX) to investigate the interactions between catalyst and scaffold prior to testing and after testing. JEOL TEM 2011 transmission electron microscopy equipped with Oxford Isis EDS detector was also used to analyse the detailed microstructure and chemical composition of the bimetallic Ni-Fe impregnated anode. The TEM samples were prepared in the following way: at first, the samples were fixed into Gatan G-1 epoxy to protect the surface structures; then the cured samples were cut and thinned to electro transparency by mechanical grinding and focused ion beam polishing.

## Results and discussion

### Configuration of the cells

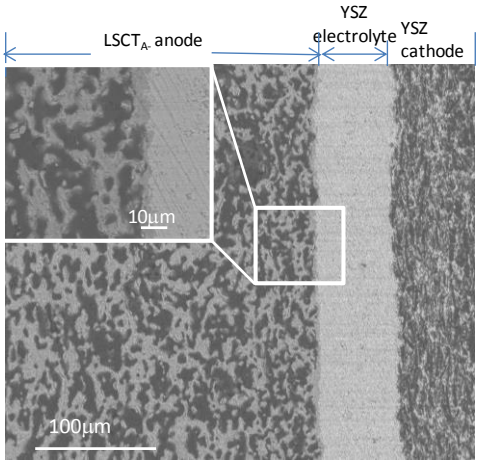


Figure 2 Back-scattered electron (BSE) image of the cross section of the cell after reduction, showing the anode to the left and the cathode to the right of the dense YSZ electrolyte. The inset is the magnified image of the anode/electrolyte interface, as shown in the rectangle.

Figure 2 shows the cross-section of a cell after the reduction at 900 $^oC$ for 12 hours and impregnation of LSCF into the YSZ cathode. It can be seen that the electrolyte is about 60-μm thick and adheres well to both cathode and anode with the average thickness of 60 and 300 μm, respectively. It was reported[29] that the chemical expansion due to the formation of larger $Ti^{3+}$

accompanied with the loss of oxygen would threaten the bonding between the anode and electrolyte. Fortunately, the microstructure indicates that neither volumetric change during the reduction at 900 $^{o}$C nor thermal cycles in air between 450 $^{o}$C and room temperature during the infiltration process did any harm to the integrity of the fuel cell. The coarse pores are observed in the anode support, which are sufficient to provide pathways for fuel transport into the functional layer at the interface of electrode and electrolyte. The inset of Figure 2 is the magnified BSE image of the electrolyte/anode interface. It demonstrates that a good intimacy has been successfully formed between the perovskite anode and the YSZ electrolyte by co-casting and co-sintering techniques. A thin but indented $LSCT_{A-}$ layer closely attached to YSZ electrolyte could provide more surface area to support the anode electrochemical reaction on the electrolyte/anode interface, where YSZ, $LSCT_{A-}$ and fuel meet together, going some way to mitigate the lack of ionic conductivity in the $LSCT_{A-}$ and promote the transport and exchange of oxygen ions from the YSZ electrolyte within the $LSCT_{A-}$ anode.

## Initial performance

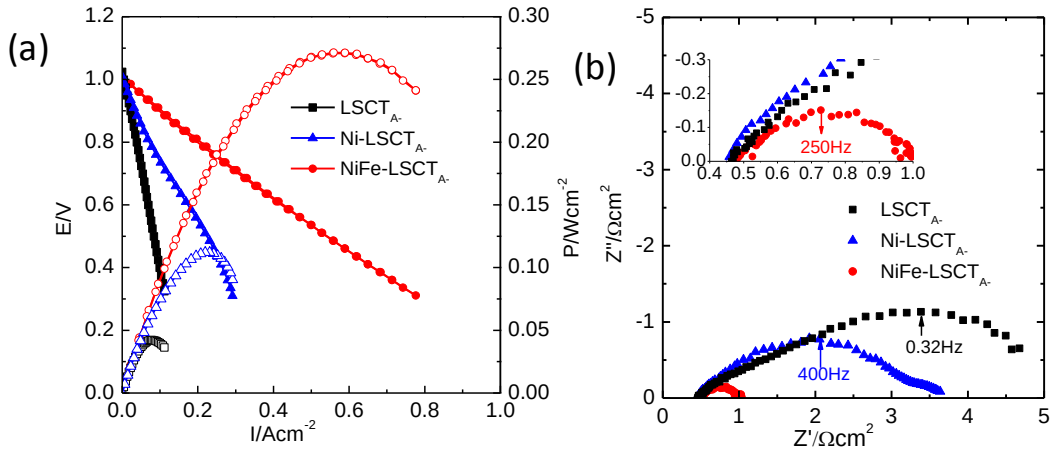


Figure 3 (a) I-V and I-P curves and (b) EIS curves of the cells tested at 700 $^{o}$C in humidified hydrogen (3 % $H_2O$) with different anodes: $LSCT_{A-}$ backbone, Ni and Ni-Fe impregnated $LSCT_{A-}$. I-V and I-P curves in (a) are signified by solid and open symbols, respectively. The inset in the Nyquist plots magnifies the high-frequency intersection with x-axis.

The initial performances of the fuel cells without catalyst, and with 3 wt.% nickel and 3 wt.% Ni-Fe on the anode at 700 $^{o}$C are shown in Figure 3. All the three cells show an open circuit voltage (OCV) of 1.02 V (Figure 3(a)), which is slightly lower than the theoretical OCV of 1.09 V from Nernst equation using humidified $H_2$ containing 3 % $H_2O$, which could related to the cross-over of gas between the cathode and anode and the low catalytic activity of the anode. The power density of the cell without catalyst showed a maximum power density of 43 mW cm$^{-2}$, and the addition of nickel to the bare $LSCT_{A-}$ anode doubles the peak power density to 112 mW cm$^{-2}$. Compared to the cell with Ni as catalyst, the substitution of 25 wt.% Fe for Ni as catalyst enhances the peak power density by a factor of 2.5 as shown in Figure 3(a), increasing from 112 mW cm$^{-2}$ to 275 mW cm$^{-2}$. According to the characteristics of the impedance spectra shown in Figure 3(b), the impedance for the cell without catalyst, with Ni and Ni-Fe catalyst was simulated using a model containing three Voigt elements in series with an ohmic resistance, $R_s$. The decrease of the $R_p$ value for impregnated

cell confirms that the high electrode losses can be attributed to the bare $LSCT_{A-}$ anode since the contribution of $R_p$ from the cathode is minor, less than 0.06 Ω $cm^2$ at 80 hours (see Figure S1 in the supplementary). This result is consistent with what has been reported for infiltrating LST[30,31], LSTM[32] and LSCM [33~35] as anodes. The simulated spectra were shown in Figure S2 and it can be seen that the three cells show a similar series resistance, $R_s$, The polarization resistance of the cell without catalyst, with Ni catalyst and Ni-Fe catalyst is 5.09, 3.22 and 0.53 Ω$cm^2$, respectively by adding up $R_1$, $R_2$ and $R_3$ (if any) for the arcs at difference frequencies. For the cell with Ni impregnated anode, three arcs with characteristeic frequencies above 1 kHz (High frequency), on the scale of 100 Hz (intermediate frequency) and below 1 Hz (low frequency) can be easily distinguished, while the cell with bare $LSCT_{A-}$ showed an merged arc at high- and intermediate frequencies. According to the previous study, the high- and intermediate-frequency arc can be assigned to the charge transfer process on the electrolyte/anode interface and the low frequency arc could be related to dissociative adsorption of gaseous species and surface diffusion.[19,36] From the simulated parameters shown in Table S1, the addition of Ni on the bare $LSCT_{A-}$ anode decreases the charge transfer process while expedites the adsorption of gaseous species and surface diffusion process and this could be related to the catalyst/$LSCT_{A-}$ interface that blocks the charge and ion transport. Surprisingly, the impedance spectra for the cell with Ni-Fe co-infiltration showed only one arc at intermediate frequency. The enhancement by impregnation of bi-metal can possibly be attributed to the better microstructure in the bi-metal system: the addition of a small amount of Fe into Ni could significantly decrease the aggregation of Ni and improve the number of active sites on Ni and the activity of those sites by decreasing the activation energy. In this case, both the charge transfer and the diffusion process are accelerated by the Fe addition[37].

## Initial stage stability test

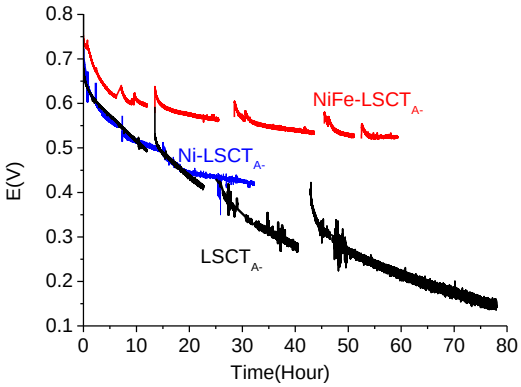


Figure 4 Time dependence of voltage of the varied anodes at 700 °C in humidified hydrogen (3% $H_2O$) under different current densities: 60, 130, and 280 mA/$cm^2$ for $LSCT_{A-}$ backbone, Ni and Ni-Fe impregnated cells, respectively.

As well as the initial performance, the chronoamperometric tests of the three cells without catalyst, and with Ni or Ni-Fe as catalyst were also examined and the voltage variations with time at current densities of 60, 130, and 280 mA/cm$^2$ for the LSCT$_{A-}$ backbone, Ni and Ni-Fe impregnated cells, respectively, at 700 $^o$C are shown in Figure 4. These current densities were set to give a starting voltage ~0.7 V, the working potential of actual SOFC, in each of the cells. The LSCT$_{A-}$ backbone shows a drastic degradation from 0.65 V to 0.15 V in 80 h, which has so far been attributed to the re-oxidation of the scaffold under relatively high oxygen partial pressure resulted from the transporting oxygen ions at the low voltages. The partial oxidation of LSCT$_{A-}$ surface causes a decrease in both ionic and electronic conductivities, and therefore results in a deterioration of the performance. The degradation rate of the cell catalyzed with pure nickel is much faster than that with nickel-iron composite. Within 32 hours, the voltage of Ni-LSCT$_{A-}$ cell drops below 0.45 V, while that of Ni-Fe composite impregnated LSCT$_{A-}$ cell stabilizes at 0.53 V after 60 hours. The prevention of the nickel aggregation by the addition of iron could be one of the reasons responsible for the improved stability[37]. The OCV of the three cells tested at intervals during the stability testing is stable, about 1.03 V, throughout the whole testing duration, which indicates the decrease of the voltage is coming from the area specific resistance of the fuel cell under constant fuel utilization. It should be noted that the performance of all the three cells slightly increases even after the short-time intermediate relaxation at OCV. It also can be seen that all the three cells show a similar degradation rate at the first 20 h, but as the time on test increases the impregnated samples demonstrate a trend to a reduced degradation rate compared to the specimen without catalyst: the presence of catalyst on the LSCT$_{A-}$ backbone prevents the further deterioration of the anode performance. The impedance spectroscopy data after the cell relaxed to OCV were simulated and the results were presented in Table S2 to S4. It can be seen that the degradation for the cell with bare LSCT$_{A-}$ and Ni catalyst is mainly from the increase of charge transfer resistance while the cell with Ni-Fe co-infiltration remains very stable. It should be noted that the addition of catalyst could be beneficial to the preservation of $R_s$ while the cell with bare LSCT$_{A-}$ is subject to the increase of ohmic resistance, and strong indication of oxidation process under bias that decreases the conductivity of the anode.

## *Ex-situ* phase stability of the catalyst

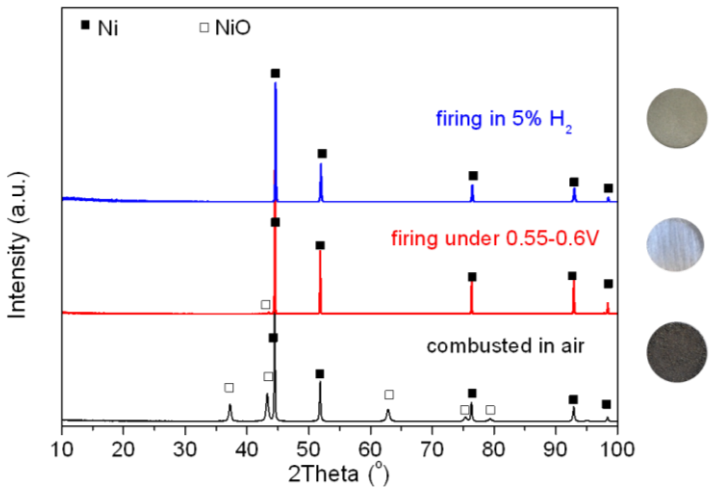


Figure 5 XRD patterns of the prepared Ni(O) powder calcined at 450 $^o$C and reduced in 5 % $H_2$-Ar or in $N_2$-$H_2$-$H_2O$ with oxygen partial pressure of $10^{-13}$ Pa (equivalent to 0.55-0.6V vs air)

The effect of different atmospheres on the phase evolution of the catalyst was of interest, so nickel nitrate solution calcined at 450 $^o$C in air for 30 min was reduced under various oxygen partial pressures for 12 h. These were a 5% $H_2$-Ar atmosphere and an oxygen partial pressure of $10^{-13}$ Pa generated by mixing $N_2$, $H_2$ and steam. As displayed in Figure 5, after annealing at 450 $^o$C, the sample is dark and composed of NiO and Ni. The formation of nickel is possibly due to the

reducing condition caused by combustion of citric acid. Upon reduction, the sample becomes brown and metallic, and is composed of a single phase of metallic nickel. Therefore, during the stability testing, the catalyst in the anode is likely to be metallic nickel rather than nickel oxide.

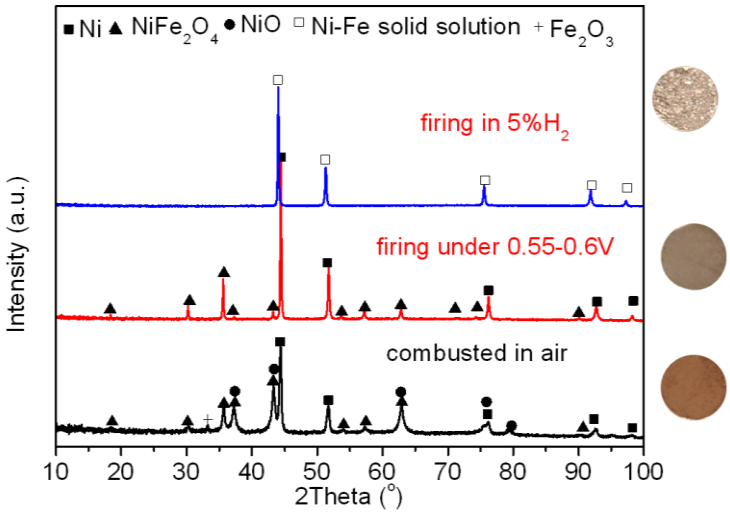


Figure 6 XRD patterns of the prepared Ni-Fe compound calcined at 450 $^{o}$C and reduced in 5 % $H_2$-Ar or in $N_2$-$H_2$-$H_2O$ with oxygen partial pressure of $10^{-13}$ Pa (equivalent to 0.55-0.6V vs air)

In order to gain a better understanding as to the effect of iron on reduction and phase composition of the catalyst under an operation equivalent atmosphere, nickel and iron nitrate solution calcined at 450 $^{o}$C in air for 30 min was subsequently reduced in either 5% $H_2$-Ar or at an oxygen partial pressure of $10^{-13}$ Pa generated by a mixture of $N_2$, $H_2$ and steam for 12h. The mole ratio of Ni to Fe in this study is 3:1. Figure 6 shows XRD patterns of Ni-Fe compound under different conditions. Before reduction, the sample powder is in brown colour on the exterior. The main phases include NiO, $NiFe_2O_4$ and Ni; however, a small diffraction peak, attributed to cubic $Fe_2O_3$ phase (JCPDs 00-002-1047), was also detected. Upon reduction in argon containing 5 % hydrogen, the sample becomes metallic colour, the diffraction peaks of which can assigned for cubic awaruite $FeNi_3$ (JCPDs 00-038-0419). However, after being reduced at the atmosphere with $P(O_2)$~$10^{-13}$ Pa, the sample is comprised of metallic nickel and spinel oxide. Therefore, during the stability testing, the catalyst in the anode is likely to maintain as metallic nickel and iron oxide rather than $FeNi_3$.

## Microstructure of the anode

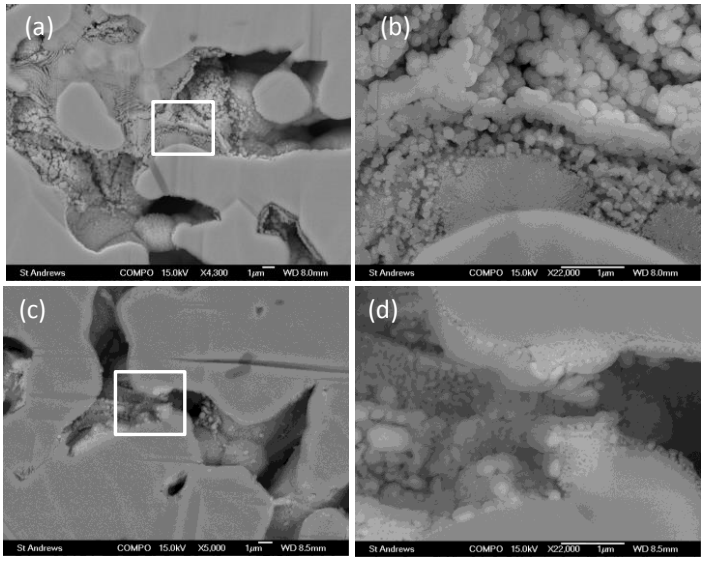

Figure 7 Back-scattered electron (BSE) images of Ni-impregnated $LSCT_{A-}$ (a, b) after firing at 450 $^{o}$C in air for 30 min and (c, d) after the stability testing at 700 $^{o}$C for 32 h in humidified hydrogen (3 % $H_2O$). (b) and (d) are the enlarged images of the rectangular areas in the general images (a) and (c), respectively.

As the addition of catalyst is shown to improve both the performance and the durability of the cell, it is therefore of interest to investigate any correlation between the performance and the microstructure of $LSCT_{A-}$-based anodes. Figure 7 shows the back-scattered electron (BSE) images of the Ni-$LSCT_{A-}$ anode before and after testing for 32 hours. From the micrographs it can be seen that after impregnation and low-temperature firing, a uniform coating of nano-sized NiO/Ni has formed on the $LSCT_{A-}$ support surface (Figure 7(a) and (b)). Fine particles, around 50 nm, can be seen on the edges around the $LSCT_{A-}$ grains, especially around the convex areas, and coarse particles, around 200 nm in diameter, are concentrated on the concave surfaces. The difference in the size of the catalyst particles is attributed to the uneven deposition process driven by capillary action, resulting in a thinner layer formed on convex surfaces and a thicker layer on concave surfaces[38]. After the initial I-V testing at 700 $^{o}$C under humidified hydrogen, Ni particles tend to dispersed on the surface of the $LSCT_{A-}$ scaffold and the size of Ni particles are on the scale of 100 nm[19] and an additional image is also provided in Figure S3. There is a significant change in the microstructure after 32 hours in humidified hydrogen at 700$^{o}$C as shown in Figure 7(c) and (d). A continuous bright layer contains nanoparticles of 50 nm, which tend to line up along the edge of $LSCT_{A-}$ grains but agglomerate on the corners (Figure 7(d)). A layer, even darker than the backbone, can be distinguished outside the bright layer, the composition of this darker layer is not yet clear. However, there is some speculation that it may be composed of backbone material as the decomposition of the nitrate and citric acid produces conditions of localised acidity and could therefore induce a partial dissolution of the backbone during the firing process followed by re-nucleation and growth during fuel cell testing. Gorte et al. has studied the deactivation of Pd on $La_{0.7}Sr_{0.3}VO_3$, and proposed that the coverage of $Sr_2V_2O_7$ on Pd surface could be the reason for the performance degradation of composite anode[39].

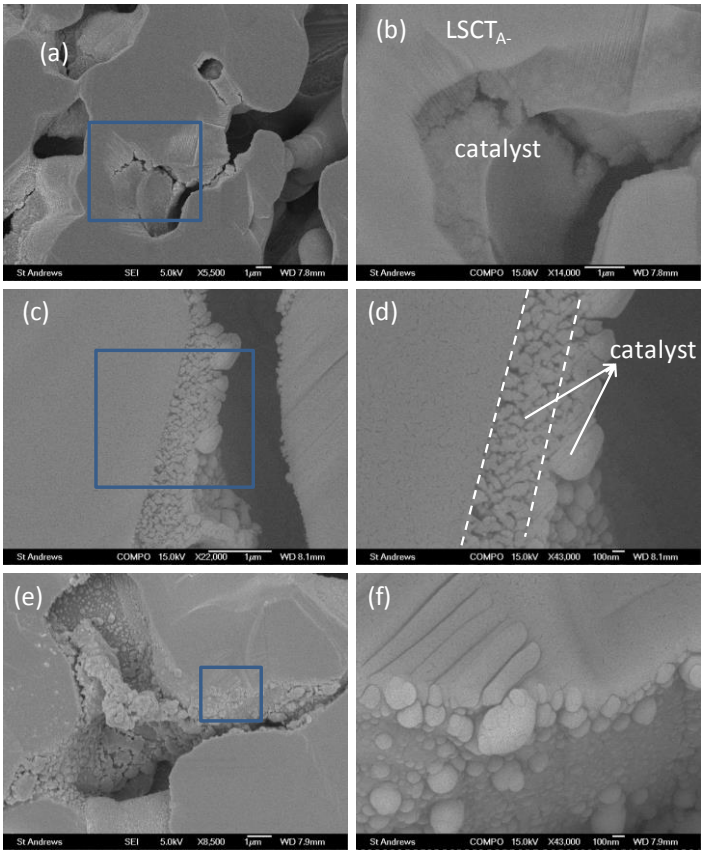


Figure 8 Secondary electron microscopy (SEM) and Back-scattered electron (BSE) images of Ni-Fe impregnated LSCT$_{A-}$ (a, b) before testing, (c, d) and (e, f) after testing for 24 and 60 h, respectively, at 700 $^{o}$C. (b), (d) and (f) the enlarged images of the rectangular areas in the general images (a), (c) and (e), respectively.

The microstructures of Ni-Fe impregnated LSCT$_{A-}$ anode at different testing times are shown in Figure 8. After firing at 450 $^{o}$C, a dense layer of bi-metallic oxide is formed covering the surface of the backbone particles (Figure 8(a)). In particular, the thickness of the catalyst can reach around 1 μm at the bottom side (Figure 8(b)). After initial I-V testing under humidified hydrogen, the catalyst layer forms a connected framework with grains under the scale of 50 nm as shown in Figure S4. The distribution of the catalyst again suggests that capillary forces play have a strong influence during the impregnation process. A comparison of the SEM image (Figure 8(a)) and BSE image (Figure 8(b)) implies a seamless bonding between the catalyst and backbone. After 24-h reduction in 5% $H_2$ at 700 $^{o}$C, the dense layers become a porous coating comprising of metallic particles of 200 nm in diameter on the very top but 50nm in diameter between top layer and the backbone (Figure 8(d)). It seems that some coarsening occurs at upper surface where the particles have greater degree of freedom for movement. With time the coarsening envelops across the entire thickness lead eventually to spalling as seen in Figures 8(e) and (f). A dark circle with thickness of 50-100 nm is detected on the surface of the large catalyst. The nature of this dark area is not certain so far, but could be oxides from the backbone due to the low molar mass per atom indicated by BSE images. To better identify any composition variation across these grains, the sample was examined using EDX on a TEM to avoid the large interaction volume of the electron beam with a thick substrate as encountered when using EDX on a SEM. From the Figure 8(e), the spalling of the thick catalyst layer after 60-h reduction may be a contributing reason for the degradation of the performance.

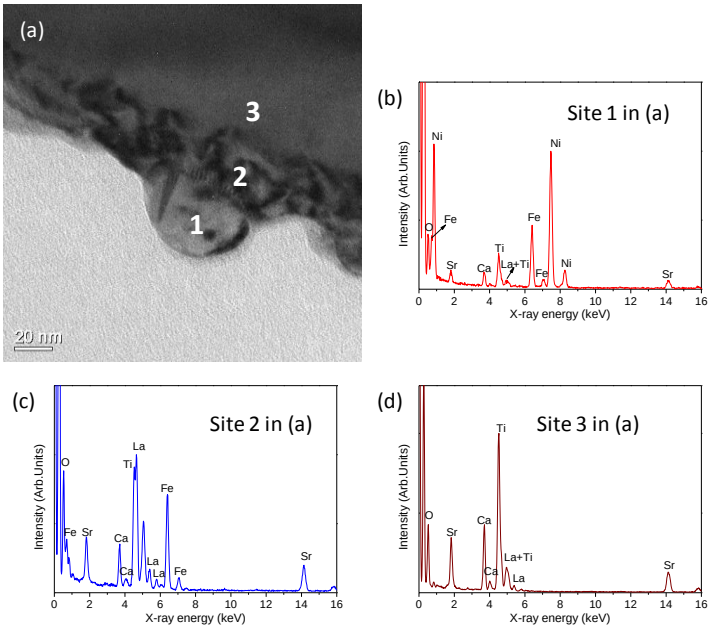


Figure 9 Transmission electron microscopy (TEM) image (a) of $LSCT_{A-}$ anode coated with a Ni-Fe layer on the surface after stability testing for 24 h at 700 $^{o}$C in humidified hydrogen and the corresponding EDX spectra (b), (c) and (d) of the marked areas by numbers 1, 2 and 3

A TEM micrograph with EDX is able to reveal more detail of impregnated catalyst on the backbone and identify the elemental composition of the different layers. The TEM image of an interface between the $LSCT_{A-}$ backbone and catalyst after testing in fuel cell condition for 24 h is shown in Figure 9, along with the corresponding EDX spectra. Two different structures on the $LSCT_{A-}$ backbone can be observed, including a nanoparticle on the very top and a relatively dense layer between the backbone and top layer, consistent with the analysis result of SEM images. According to the EDX spectra of the coating, there is chemical interaction between Ni-Fe and $LSCT_{A-}$ backbone. The microstructure of the catalyst on the $LSCT_{A-}$ surface plays an important role in the cell performance: on the very top the nanoparticle is mainly comprised of Ni (63 at. % of the cation) and Fe(28 at.% of the cation) with minor La, Sr and Ti; the layer between Ni-Fe nanoparticles and $LSCT_{A-}$ backbone, as indicated by site 2, shows a strong interaction between iron and the backbone, consisting of possibly $(La,Sr,Ca)_2Fe(Ti)O_4$ and/or $La(Sr,Ca)Fe(Ti)O_3$ and titanate since the atomic percentage of the cation in this layer contains 46 % La, 33 % Fe, 8% Sr, 7 % Ca and 7% Ti in atomic ratio. The ceramic interlayer could also serve as an coating that retards the oxidation of underneath $LSCT_{A-}$ anode, which could be implied from the stable $R_s$ value of the cell during testing under bias for different times. The growth of nano-sized metallic catalyst particles due to thermal instability is always attributed to be the major reason for the performance degradation of a cell prepared with infiltration[40]. The nano particle growth has two ramifications: it will decrease the surface area for electrochemical reactions and in electrodes where the infiltrated phase supplies electrical conductivity, and increase the series resistance by creating larger intergranular gaps and eventual loss of percolation. In this particular anode-supported cell arrangement where the $LSCT_{A-}$ support structure provides most of the electrical conductivity, the bulk of the degradation will mostly likely come from the reduction of surface area for catalysis. The growth of metal particles is obvious from the SEM images, but the interaction between the metal particles and the $LSCT_{A-}$ backbone may contribute to a further degradation mechanism for the anode. The substitution of Fe for Ni may be able to decrease the particle size growth due to the existence of iron-containing oxides interacting with the backbone and to a lesser extent, this interaction of Ni-Fe catalyst with the $LSCT_{A-}$ backbone could also decrease the coverage of backbone oxide on the catalyst surface.

## Conclusions

The fuel cells using A-site deficient strontium titanate $La_{0.2}Sr_{0.25}Ca_{0.45}TiO_3$ ($LSCT_{A-}$) as an anode scaffold material reduced at high temperature (i.e. 900$^oC$) show a promising electrochemical performance after impregnation of catalyst. The impregnation of a bimetal Ni-Fe catalyst has been shown to improve the electrochemical performance compared with a cell impregnated with only Ni. Possible mechanisms for this improvement could be due to an optimized microstructure of the catalyst as the Fe addition improves the number of active sites on Ni and the activity of those sites by decreasing the activation energy, leading to an accelerated charge transfer and the diffusion process.

The impregnated samples demonstrate a more stable performance than those without catalyst during testing in humidified hydrogen for 60 h, however they still show some performance degradation with time. This is most likely linked to the significant microstructural evolution observed in the impregnated cells before and after testing. The growth of catalyst particles and the interaction between the catalyst and $LSCT_{A-}$ backbone are likely to be the main reasons for the degradation of the cell performance. As well as improving electrochemical performance the combined Ni-Fe catalyst was also shown to effectively reduce degradation when compared with the pure nickel catalyst as the agglomeration and growth of the particles has been slowed by the addition of Fe, and the chemical interaction between nickel catalyst on the outer layer and $LSCT_{A-}$ backbone has also been inhibited by the Fe-rich layer on the inner layer attached to the anode backbone.

**Acknowledgements**

The research leading to these results has received funding from the European Union's Seventh Framework Programme (FP7/2007-2013) for the Fuel Cells and Hydrogen Joint Technology Initiative under grant agreement n° 256730 and Energy Technology Partnership (ETP). We would also like to thank Stewart McCracken of MCS Ltd Edinburgh for access to the Leica EM TIC 3X Triple Ion Beam System for sample preparation as part of the ETP PhD Studentship.

**References**

[1] T. Setoguchi, K. Okamoto, K. Eguchi and H. Arai, *J. Electrochem. Soc.*, 1992, **139**, 2875-2880
[2] S. P. Jiang, *Int. J. Hydrogen Energy*, 2012, **37**, 449-470
[3] A. Atkinson, S. Barnett, R. J. Gorte, J. T. S. Irvine, A. J. Mcevoy, M. Mogensen, S. C. Singhal and J. Vohs, *Nat. Mater.*, 2004, **3**, 17-27
[4] L. Yang, S. Wang, K. Blinn, M. Liu, Z. Liu, Z. Cheng and M. Liu, *Science*, 2009, **326**, 126-129
[5] L. Yang, Y. Choi, W. Qin, H. Chen, K. Blinn, M. Liu, P. Liu, J. Bai, T. A. Tyson and M. Liu, *Nat. Commun*, 2011., **2**, 357-365
[6] S. T. Aruna, M. Muthuraman and K. C. Patil, *Solid State Ionics*, 1998, **111**, 45-51
[7] J. H. Lee, H. Moon, H. W. Lee, J. Kim, J. D. Kim and K. H. Yoon, *Solid State Ionics*, 2002, **148**, 15-26
[8] M. L. Toebes, J. H. Bitter, A. J. van Dillen and K. P. de Jong, *Catal. Today*, 2002, **76**, 33-42
[9] Y. Matsuzaki and I. Yasuda, *Solid State Ionics*, 2000, **132**, 261-269
[10] T. Iwata, *J. Electrochem. Soc.*, 1996, **143**, 1521-1525
[11] P. R. Slater, D. P. Fagg and J. T. S. Irvine, *J. Mater. Chem.*, 1997, **7**, 2495-2498
[12] Q. X. Fu, S. B. Mi, E. Wessel and F. Tietz, *J. Eur. Cera. Soc.*, 2008, **28**, 811-820
[13] R. Mukundan, E. L. Brosha and F. H. Garzon, *Electrochem. Solid-State Lett.*, 2004, **7**, A5-A7
[14] Q. Ma, F. Tietz, *Solid State Ionics*, 2012, **225**, 108-112
[15] O. A. Marina, N. L. Canfield, J. W. Stevenson, *Solid State Ionics*, 2002, **149**, 21-28
[16] K. B. Yoo and G. M. Choi, *Solid State Ionics*, 2009, **180**, 867-871
[17] Q. L. Ma, F. Tietz, A. Leonide and E. Ivers-Tiffee, *J. Power Sources*, 2011, **196**, 7308-7312
[18] C. D. Savaniu and J. T. S. Irvine, *J. Mater. Chem.*, 2009, **19**, 8119-8128

[19] L. Lu, C. Ni, M. Cassidy and J. T. S. Irvine, *J. Mater. Chem. A*, 2016, **4**, 11708-11718
[20] S. Lee, N. Miller and K. Gerdes, *J. Electrochem. Soc.*, 2012, **159**, F301-F308
[21] W. Wang,M. D. Gross, J. M. Vohs and R. J. Gorte, *J. Electrochem. Soc.*, 2007, **154**, B439-445
[22] C. Setevich, F. Prado, D. Z. de Florio and A. Caneiro, *J. Power Sources*, 2014, **247**, 264-272
[23] Y. Liu, F. Wang, B. Chi, J. Pu, L. Jian and S. P. Jiang, *J. Alloy Compd.*, 2013, **578**, 37-43
[24] Q. Ma, B. Iwanschitz, E. Dashjav, A. Mai, F. Tietz, H.-P. Buchkremer, *Solid State Ionics*, 2014, **262**, 465-468
[25] Q. Ma, B. Iwanschitz, E. Dashjav, S. Baumann, D. Sebold, I. A. Raj, A. Mai, F. Tietz, *J. Power Sources*, 2015, **279**, 678-685
[26] M. C. Verbraeken, B. Iwanschitz, E. Stefan, M. Cassidy, U. Weissen, A. Mai and J. T. S. Irvine, Fuel Cells, 2015, **15**, 682-688
[27] R. Küngas, J.-S. Kim, J. M. Vohs and R. J. Gorte, *J. Am. Ceram. Soc.*, 2011, **94**, 2220-2224
[28] J. T. S. Irvine, D. Neagu, M. C. Verbraeken, C. Chatzichristodoulou, C. Graves and M. B. Mogensen, *Nat. Energy*, 2016, **1**, 15014
[29] D. Marrocchelli, S. R. Bishop, H. L. Tuller and B. Yildiz, *Adv. Funct. Mater.*, 2012, **22**, 1958-65
[30] S. Lee, G. Kim, J. M. Vohs and R. J. Gorte, *J. Electrochem. Soc.*, 2008, **155**, B1179-B1183
[31] J. S. Park, I. D. Hasson, M. D. Gross, C. Chen, J. M. Vohs and R. J. Gorte, *J. Power Source*, 2011, **196**, 7488-7494
[32] J. H. Kim, H. Schlegl and J. T. S. Irvine, *Int. J. Hydrogen Energy*, 2012, **37**, 14511-14517
[33] J. S. Kim, V. V. Nair, J. M. Vohs and R. J. Gorte, *Scripta Mater.*, 2011, **65**, 90-95
[34] G. Kim, S. Lee, J. Y. Shin, G. Corre, J. T. S. Irvine, J. M. Vohs and R. J. Gorte, *Electrochem. Solid-State Lett.*, 2009, **12**, B48-B52
[35] G. Kim, G. Corre, J. T. S. Irvine, J. M. Vohs and R. J. Gorte, *Electrochem. Solid-State Lett.*, 2008, **11**, B16-B19
[36] M. C. Verbraeken, B. Iwanschitz, A. Mai and J. T. S. Irvine, J. Electrochem. Soc., 2012, **159**, F757-F762.
[37] T. Ishihara and H. Zhong, Effects of Fe addition on the surface reaction of the anode of intermediate temperature solid oxide fuel cells, *Scripta Mater.*, 2011, **65**, 108-111
[38] G. Corre, G. Kim,, M. Cassidy, J. M. Vohs, R. J. Gorte and J. T. S. Irvine, *Chem. Mater.*, 2009, **21**, 1077-1084
[39] J.–S. Park, J. Luo, L. Adijanto, J. M. Vohs and R. J. Gorte, *J. Power Sources*, 2013, **222**, 123-128
[40] S. Jung, C. Lu, H. He, K. Ahn, R. J. Gorte and J. M. Vohs, *J. Power Sources*, 2006, **154**, 42-50

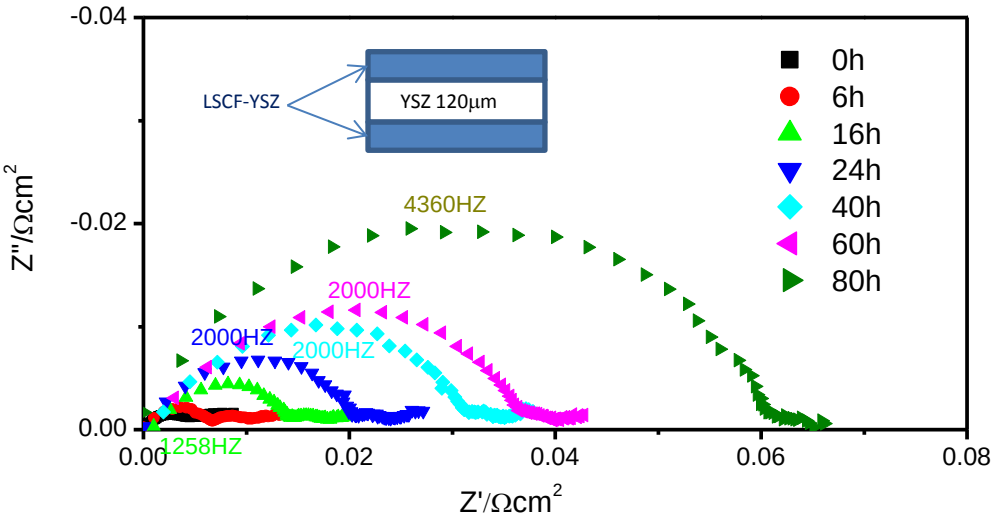


Figure S1 The polarization resistance of the symmetrical LSCF-YSZ cathode with time tested at 700 °C in air.

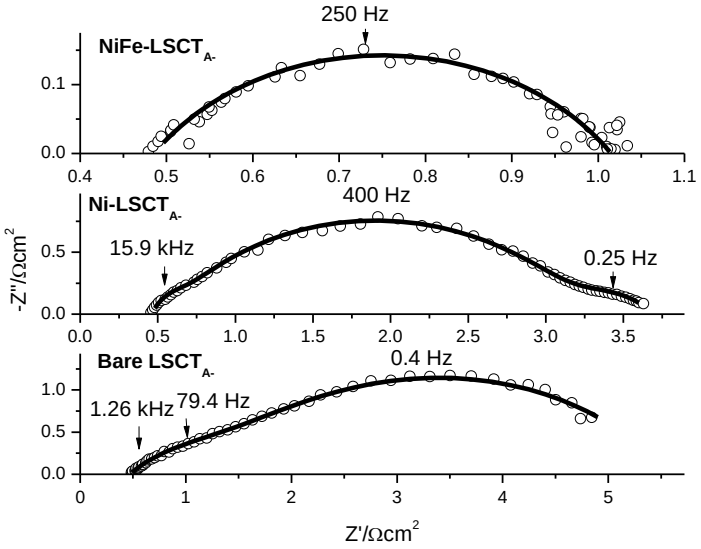


Figure S2 The experimental (open symbols) and simulated (line) EIS results of the three cells under OCV tested at 700 °C in 3% $H_2O$-$H_2$.

Table S1 Parameters from the simulated EIS data of the three cells tested at 700 °C. The three cells have been fitted with the equivalent circuit $R_s(R_1Q_1)(R_2Q_2)(R_3Q_3)$, where n and Q are parameters associated with constant phase element. The units of R and Q are Ω cm$^2$ and $\Omega^{-1}s^n$ cm$^{-2}$, respectively.

| | $R_s$ | $Q_1$ | $n_1$ | $R_1$ | $Q_2$ | $n_2$ | $R_2$ | $Q_3$ | $n_3$ | $R_3$ |
|---|---|---|---|---|---|---|---|---|---|---|
| **$LSCT_{A-}$** | 0.47 | | | | $5.74\times10^{-2}$ | 0.53 | 1.08 | $1.59\times10^{-1}$ | 0.63 | 4.01 |
| **Ni-$LSCT_{A-}$** | 0.46 | $1.69\times10^{-4}$ | 1.00 | 0.12 | $5.22\times10^{-3}$ | 0.66 | 2.59 | 1.16 | 0.61 | 0.51 |
| **NiFe-$LSCT_{A-}$** | 0.49 | | | | $2.11\times10^{-2}$ | 0.63 | 0.53 | | | |

Table S2 Parameters from the simulated EIS data of the bare $LSCT_{A-}$ cell tested at 700 °C with time. The data have been fitted with the equivalent circuit $R_s(R_2Q_2)(R_3Q_3)$, where n and Q are parameters associated with constant phase element.

| | | Time /h | | | |
|---|---|---|---|---|---|
| Parameter | Unit | 0 | 12 | 24 | 40 |
| $R_s$ | $\Omega$ cm$^2$ | 0.47 | 0.58 | 0.69 | 0.75 |
| $Q_2$ | $\Omega^{-1}$ s$^n$ cm$^{-2}$ | 5.75x10$^{-2}$ | 5.29 x10$^{-2}$ | 5.14 x10$^{-2}$ | 4.42 x10$^{-2}$ |
| $n_2$ | | 0.53 | 0.51 | 0.49 | 0.50 |
| $R_2$ | $\Omega$ cm$^2$ | 1.08 | 1.28 | 1.62 | 1.42 |
| $Q_3$ | $\Omega^{-1}$ s$^n$ cm$^{-2}$ | 0.16 | 0.15 | 0.15 | 0.15 |
| $n_3$ | | 0.63 | 0.60 | 0.67 | 0.68 |
| $R_3$ | $\Omega$ cm$^2$ | 4.00 | 6.38 | 3.04 | 2.49 |

Table S3 Parameters from the simulated EIS data of the Ni- $LSCT_{A-}$ cell tested at 700 °C with time. The data have been fitted with the equivalent circuit $R_s(R_1Q_1)(R_2Q_2)(R_3Q_3)$, where n and Q are parameters associated with constant phase element.

| | | Time /h | | |
|---|---|---|---|---|
| Parameter | Unit | 0 | 40 | 46 |
| $R_s$ | $\Omega$ cm$^2$ | 0.46 | 0.53 | 0.33 |
| $Q_1$ | $\Omega^{-1}$ s$^n$ cm$^{-2}$ | 1.68x10$^{-4}$ | 2.00 x10$^{-4}$ | 2.05 x10$^{-4}$ |
| $n_1$ | | 1.00 | 0.23 | 0.38 |
| $R_1$ | $\Omega$ cm$^2$ | 0.12 | 0.05 | 0.27 |
| $Q_2$ | $\Omega^{-1}$ s$^n$ cm$^{-2}$ | 5.19 x10$^{-3}$ | 9.53 x10$^{-3}$ | 9.03 x10$^{-3}$ |
| $n_2$ | | 0.66 | 0.51 | 0.51 |
| $R_2$ | $\Omega$ cm$^2$ | 2.61 | 5.45 | 5.61 |
| $Q_3$ | $\Omega^{-1}$ s$^n$ cm$^{-2}$ | 1.16 | 1.77 | 1.75 |
| $n_3$ | | 0.61 | 0.99 | 1.00 |
| $R_3$ | $\Omega$ cm$^2$ | 0.51 | 0.45 | 0.49 |

Table S4 Parameters from the simulated EIS data of the NiFe- $LSCT_{A-}$ cell tested at 700 °C with time. The data have been fitted with the equivalent circuit $R_s(R_2Q_2)$, where n and Q are parameters associated with constant phase element.

| | | Time /h | | | | |
|---|---|---|---|---|---|---|
| Parameter | Unit | 0 | 12 | 24 | 40 | 56 |
| $R_s$ | $\Omega$ cm$^2$ | 0.49 | 0.44 | 0.46 | 0.48 | 0.50 |
| $Q_2$ | $\Omega^{-1}$ s$^n$ cm$^{-2}$ | 2.11x10$^{-2}$ | 5.68 x10$^{-2}$ | 5.78 x10$^{-2}$ | 5.27 x10$^{-2}$ | 4.52 x10$^{-2}$ |
| $n_2$ | | 0.63 | 0.52 | 0.52 | 0.52 | 0.54 |
| $R_2$ | $\Omega$ cm$^2$ | 0.53 | 1.48 | 1.55 | 1.52 | 1.52 |

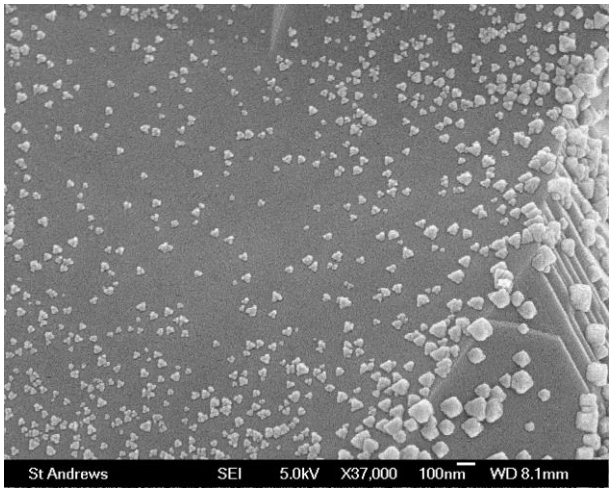


Figure S3 SEM of the Ni infiltrated $LSCT_{A-}$ anode after initial I-V testing at 700 $^{o}$C.

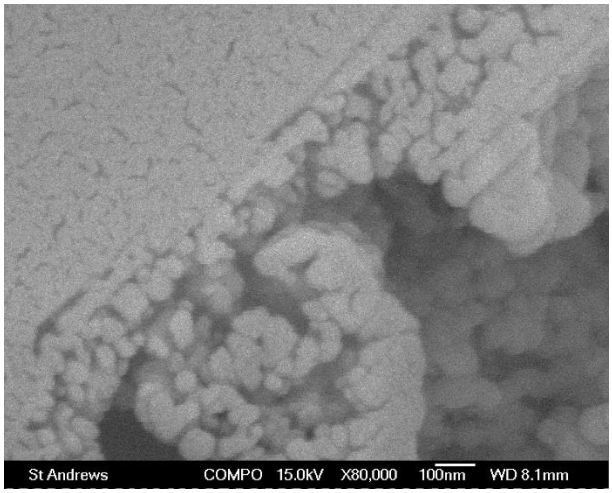


Figure S4 SEM of the Ni-Fe infiltrated $LSCT_{A-}$ anode after initial I-V testing at 700 $^{o}$C.